

Supporting Information:

“Self-assembly within an oscillatory energy landscape: orderly assembly depends on the interplay between time-dependent potential and intrinsic relaxation time-scales.”

Jessica K. Niblo,[†] Jacob R. Swartley,[†] Zhongmin Zhang,[‡] and Kateri H. DuBay^{*,†}

[†]*Department of Chemistry, University of Virginia, Charlottesville, VA*

[‡]*Department of Chemistry, University of North Carolina at Chapel Hill, Chapel Hill, NC*

E-mail: dubay@virginia.edu

S1 Additional Methods Details

S1.1 Particle and Inter-particle Interactions Details

The triangular particles are composed of fifteen, partially overlapping circular subparticles that are rigidly held together. Each triangular edge is composed of six subparticles, the outermost of which serve as the vertices of the triangular particle and are shared with the neighboring edge. The triangular particles have an edge length of 1σ , while the subparticles have a diameter of $\sigma_{LJ} = 0.25\sigma$, where σ is the lengthscale of the system in reduced units.

The subparticles on two edges of the equilateral triangle are assigned type A, while the subparticles on the third edge (including their vertices) are assigned type B. The type

A - type A subparticles of differing triangular particles interact via a Lennard-Jones (LJ) potential, which is illustrated in Figure 1a, and defined as:

$$V_{\text{LJ}}(r_{ij}) = 4\epsilon_{ij}\left[\left(\frac{\sigma_{\text{LJ}}}{r_{ij}}\right)^{12} - \left(\frac{\sigma_{\text{LJ}}}{r_{ij}}\right)^6\right] + c \quad r_{ij} < r_c, \quad (\text{S1})$$

where r_{ij} is the distance between the centers of an ij -pair, σ_{LJ} is the distance in which the potential goes to zero, and ϵ is the depth of the potential well. For static simulations, ϵ is held constant throughout the simulation, while ϵ is oscillated in time during oscillatory simulations as detailed in the main text. c is the value necessary to shift the potential so that $V_{\text{LJ}}(r_c) = 0$. For type A subparticles, σ_{LJ} defines the spatial extent of the LJ interaction, and the cutoff distance is set so that $r_c = 2.5\sigma_{\text{LJ}}$.

The type B - type B and type A - type B subparticles interact via the Weeks-Chandler-Anderson potential,^{S1} which truncates and shifts the LJ potential given in Equation S1 to only include the repulsive portion of the curve where $\frac{\partial U_{ij}(r)}{\partial r} < 0$. In order to truncate and shift the potential, we set $\epsilon_{AB} = \epsilon_{BB} = 1.0$ and $r_c = 2^{1/6}\sigma_{\text{LJ}}$.

S1.2 Simulation Details

All simulations are performed using Langevin dynamics, as implemented in LAMMPS.^{S2} Simulations started with a randomly distributed system of 150 triangular particles in a periodic box of size $L \times L$ with no particle overlap. Simulations with a volume fraction of $\phi = 0.1$ were done in a box with dimensions $25.48\sigma \times 25.48\sigma$, while simulations at a volume fraction of $\phi = 0.005$ occurred in a box with dimensions of $113.98\sigma \times 113.98\sigma$.

To relax the system, initial velocities were assigned and the simulation was allowed to equilibrate for 1,000,000 steps ($5,000\tau$). During this process, all subparticles interacted via the WCA potential, as this ensures there is no particle overlap and establishes an equilibrated random distribution of triangles. After equilibration, the type A attractive interactions were turned on, and the simulation was allowed to proceed for 30,000,000 steps ($150,000 \tau$).

Simulations were evolved in time using the velocity-Verlet algorithm with a timestep of 0.005τ . To mimic solvent dynamics and maintain a constant temperature, the Langevin thermostat was used. The Langevin equation is defined as

$$m \frac{dv}{dt} = -\gamma v - \frac{dU}{dr} + \eta(t). \quad (\text{S2})$$

In addition to the conservative force, $-\frac{dU}{dr}$, that arises from the inter-particle interactions, each triangular particle experiences a friction force and a random force. The friction force is defined as $-\gamma v$, where γ tunes the strength of the friction and v is the velocity describes the frictional interaction between the implicit solvent and the particles. In LAMMPS, we set γ by the *damp* parameter, with $damp = \frac{m}{\gamma}$, where m is mass.^{S2} We set $damp = 0.35$ in reduced units. The random force, $\eta(t)$ in Equation S2, mimics the random bumps and kicks the solvent atoms will provide to the subparticle at temperature T . The LAMMPS code was modified so that it used a Gaussian random number for $\eta(t)$ to ensure the appropriate fluctuation statistics.

S1.3 Data Analysis Details

Once the attractive LJ interactions have been turned on, atom positions are recorded every 10τ to monitor the progression of the self-assembly process. To have an even sampling while calculating the final yields, the final $7,500\tau$ of each simulation is sampled every 15τ in the static system.

In the temporally variant system, however, sampling the system with a constant interval will result in uneven sampling of the system as it switches between ϵ_{\min} and ϵ_{\max} . To ensure even sampling between the ϵ_{\min} and ϵ_{\max} half-cycles during the calculation, the last $7,500\tau$ of the simulations is divided into slices of 150τ and ten evenly spaced snapshots from the first complete period of each slice were recorded. For periods equal to or shorter than 0.05τ (ten steps), every step of the first complete period of each slice was recorded to evenly monitor

time within the ϵ_{\min} and ϵ_{\max} half-cycles.

S1.3.1 Capsid Counting

To determine the number of assembled capsids, the locations of the type A subparticles that are positioned at the attractive vertex of each triangular particle are compared to the attractive vertices of the other nearby triangular particles. We consider two triangular particles to be part of a potential capsid if the distance between the centers of their attractive vertices are less than 0.85σ . A distance less than 0.85σ was determined to encompass the fluctuations possible in the capsid shape. If any subparticle tip is found to have five neighboring subparticle tips within a distance of 0.85σ , the capsid is considered assembled.

S1.3.2 Aggregate Counting

We also analyze the number of other aggregate structures to better understand the overall assembly process. After determining the number of capsids within the system, the particles that are not within assembled capsids are analyzed to determine what size aggregate they are assembled into. We compare the three vertices of each triangular particle with the three vertices of the nearby particles to determine if the maximum length between any two vertices is less than 2.1σ . A maximum distance of 2.1σ ensures that two particles are assembled, but accounts for all configurations the particles can take in the snake-like aggregates. Aggregates are then built by noting which particles belong to each aggregate.

S2 Temperature in the intermediate period regime

Langevin Dynamics is utilized to move the simulation forward in time and maintain a constant temperature. In LAMMPS,^{S2} a Langevin parameter, $damp = \frac{m}{\gamma}$ where m is the mass of the triangular body and γ tunes the frictional strength, is defined in units of τ and determines how rapidly the temperature is relaxed to the target temperature. In this work, we

set $damp = 0.35\tau$.

For oscillation periods similar to the timescale of the damp parameter (0.35τ), the average temperature of the simulation is higher than the target temperature of 1.0. Figure S1 shows the average temperatures observed in the simulations over the last $5,000\tau$ for a range of oscillation periods compared to the average temperature for the static potential system. Temperatures at the fast oscillation limit and at oscillations great than 10τ are comparable to the static system, and periods within an intermediate range from 0.04τ to 5τ are outside a 5% error of the target temperature.

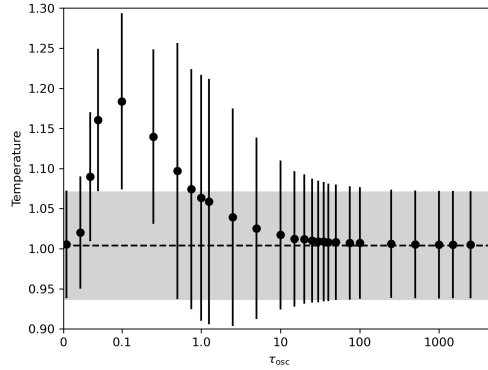


Figure S1: Average temperature for $\epsilon = 1.25k_B T$. The average temperature and its standard deviation over the last $5,000\tau$ of the simulation is plotted vs. the oscillation period τ_{osc} . The average static temperature is represented by a black dashed horizontal line, and the grey shaded region indicates its standard deviation. We present the average temperatures at $\epsilon = 1.25k_B T$ for an amplitude of $0.4k_B T$ as this value is closest to the median ϵ value observed in Figure 5b.

Due to the nature of the Lennard-Jones potential, an increased sampling temperature requires an increased ϵ value for orderly assembly to emerge. To standardize our results for an average ϵ value over the full range of oscillation periods, we scale ϵ_{avg} by the observed average temperature ($\frac{\epsilon_{avg}}{T_{avg}}$) to scale the system to represent the behavior for a time averaged temperature of 1.0. This rescaling was only performed for Figure 5 as other figures do not include results from oscillation periods between 0.04τ to 5τ .

S3 Kinetic traces of structure formation within the static system from $\epsilon = 0.75k_B T$ to $\epsilon = 2.15k_B T$.

In Figure S2 we expand Figure 2b to include additional interaction strengths.

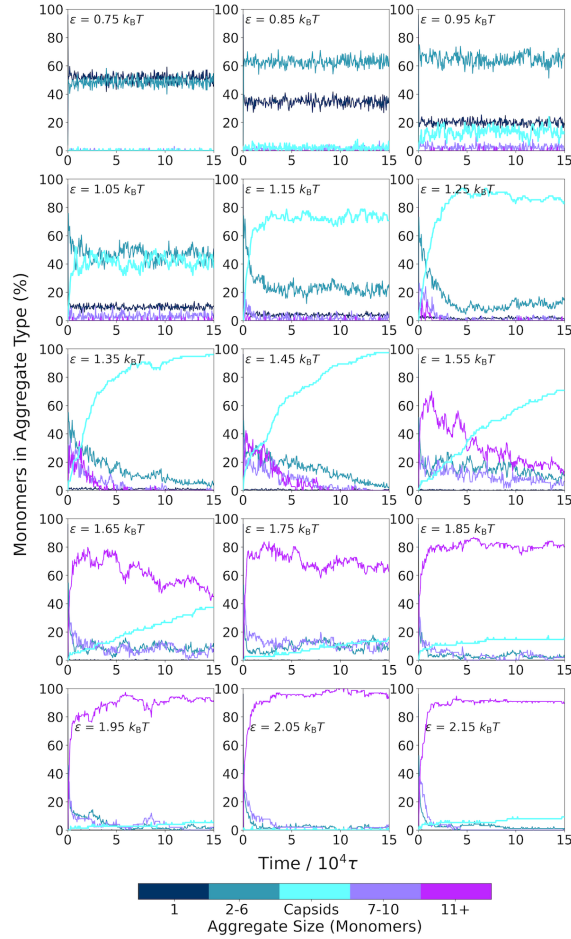


Figure S2: Formation of capsids and aggregates vs. time for different ϵ values in the non-oscillatory system. The formation of various aggregate and capsid species is plotted here vs. time for different ϵ values over a simulation time of $150,000\tau$. The different aggregate sizes are indicated by the color bar, and the kinetic traces are the average of three independent trajectories.

S4 Mean square displacement and rotational relaxation of a single triangular particle.

We examine the interplay between the oscillation period and the time it takes to diffuse characteristic length-scales that characterize important energetic and structural changes. To quantify particle diffusion, we calculate the mean square displacement for a lone triangle and plot it vs. simulation time in Figure S3a. Additionally, we calculate the rotational autocorrelation function and plot it against simulation time in Figure S3b. The timescales needed to traverse characteristic distances and rotation are presented in Table 1.

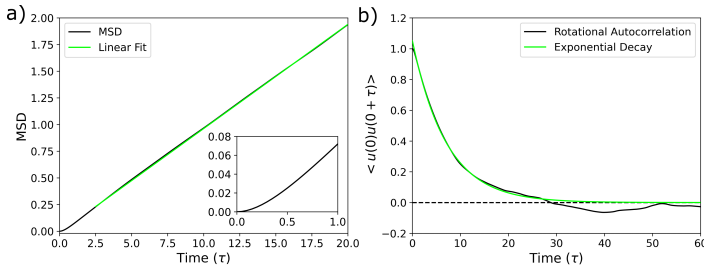


Figure S3: Mean square displacement and orientational autocorrelation function for a single particle. a) The mean square displacement is plotted vs. simulation time for a single triangular particle. Based on the linear fit line in green and the Einstein relation, the diffusion coefficient was calculated to be $D = 0.024 \pm 0.007\sigma^2/\tau$. b) The rotational autocorrelation function for a single triangular particle fit with $N(t) = N_0 \exp(-t/\tau)$, where $\tau = 7.103\tau$, and describes the time to decay to $1/e * N_0$. The mean square displacement and rotational autocorrelation function were both calculated from 18 individual trajectories with a recording interval of 0.05τ .

S5 Time averaging in the fast oscillation limit.

Based on earlier work theoretical work by Szeleifer and coworkers,^{S3,S4} the effective potential in our system can be described at the fast oscillation limit by a static LJ potential with a well depth of ϵ_{avg} , which is simply the time-dependent ϵ value averaged over a single oscillation period.

To show this correspondence, we first write the effective potential at the fast oscillation

limit as:

$$U^{\text{eff}}(r) = \int_0^{\tau_{\text{osc}}} U(r, \epsilon(t)) dt, \quad (\text{S3})$$

where $U(r, \epsilon(t))$ is the time dependent potential energy of the system at time t , which is integrated over a single oscillation period, τ_{osc} .^{S3} We can then substitute in the full LJ potential with a time dependent ϵ on the right hand side, such that:

$$U^{\text{eff}}(r) = \int_0^{\tau_{\text{osc}}} 4\epsilon(t) \left[\left(\frac{\sigma}{r} \right)^{12} - \left(\frac{\sigma}{r} \right)^6 \right] dt. \quad (\text{S4})$$

At the fast oscillation limit, any changes to r during a single oscillation period are small. As a result, Equation S4 becomes

$$\begin{aligned} U^{\text{eff}}(r) &= 4 \left[\left(\frac{\sigma}{r} \right)^{12} - \left(\frac{\sigma}{r} \right)^6 \right] \int_0^{\tau_{\text{osc}}} \epsilon(t) dt \\ &= 4 \langle \epsilon \rangle_{\tau_{\text{osc}}} \left[\left(\frac{\sigma}{r} \right)^{12} - \left(\frac{\sigma}{r} \right)^6 \right], \end{aligned} \quad (\text{S5})$$

where $\langle \epsilon \rangle_{\tau_{\text{osc}}}$ is the time averaged attraction strength over a single period, which we term ϵ_{avg} .

Finally, since in our simulations, half the oscillation period is spent at ϵ_{max} and half at ϵ_{min} ,

$$\langle \epsilon \rangle_{\tau_{\text{osc}}} = \frac{\epsilon_{\text{max}} + \epsilon_{\text{min}}}{2} = \epsilon_{\text{avg}}. \quad (\text{S6})$$

S6 Kinetic traces of structure formation with both static and oscillatory interactions.

To investigate in more detail how assembly mechanisms change with oscillatory interactions, in Figure S4 we compare the kinetic traces of the aggregate species in the static system (Column 1) to kinetic traces in the oscillatory system at three different periods. An oscillation period of 0.02τ , which is within the fast oscillation limit, results in very similar assembly

to the non-oscillatory system. Intermediate periods, shown in Columns 3 and 4, however, result in very different aggregate assembly kinetics.

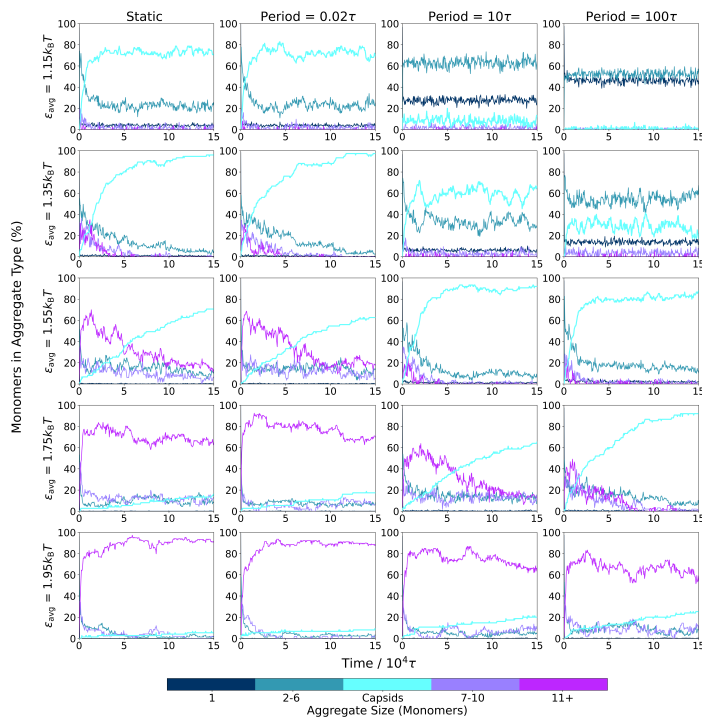


Figure S4: Formation of aggregate species over time for different oscillation periods. The formation of various aggregate species averaged over three independent trajectories is shown over time for different ϵ values and oscillation periods at an amplitude of $0.4k_B T$. Column 1 shows results from the static potential system, Column 2 shows results from the fast oscillation limit, and Columns 3 and 4 show results from two different intermediate periods. Different assembled structures are tracked over the simulation as indicated by the color bar.

References

- (S1) Weeks, J. D.; Chandler, D.; Andersen, H. C. Role of Repulsive Forces in Determining the Equilibrium Structure of Simple Liquids. *The Journal of Chemical Physics* **1971**, *54*, 5237–5247, DOI: 10.1063/1.1674820.
- (S2) Plimpton, S. Fast Parallel Algorithms for Short-Range Molecular Dynamics. *Journal of Computational Physics* **1995**, *117*, 42, DOI: 10.1006/jcph.1995.1039.

- (S3) Tagliazucchi, M.; Weiss, E. A.; Szeifer, I. Dissipative Self-Assembly of Particles Interacting through Time-Oscillatory Potentials. *Proceedings of the National Academy of Sciences* **2014**, *111*, 9751–9756, DOI: 10.1073/pnas.1406122111.
- (S4) Tagliazucchi, M.; Szeifer, I. Dynamics of Dissipative Self-Assembly of Particles Interacting through Oscillatory Forces. *Faraday Discussions* **2016**, *186*, 399–418, DOI: 10.1039/C5FD00115C.

2D capsid formation within an oscillatory energy landscape: orderly self-assembly depends on the interplay between a dynamic potential and intrinsic relaxation times.

Jessica K. Niblo,[†] Jacob R. Swartley,[†] Zhongmin Zhang,[‡] and Kateri H. DuBay*,[†]

[†]*Department of Chemistry, University of Virginia, Charlottesville, VA*

[‡]*Department of Chemistry, University of North Carolina at Chapel Hill, Chapel Hill, NC*

E-mail: dubay@virginia.edu

Abstract

Multiple dissipative self-assembly protocols designed to create novel structures or to reduce kinetic traps have recently emerged. Specifically, temporal oscillations of particle interactions have been shown effective at both aims, but investigations thus far have focused on systems of simple colloids or their binary mixtures. In this work, we expand our understanding of the effect of temporally oscillating interactions to a two-dimensional coarse-grained viral capsid-like model that undergoes a self-limited assembly. This model includes multiple intrinsic relaxation times due to the internal structure of the capsid subunits and, under certain interaction regimes, proceeds via a two-step nucleation mechanism. We find that oscillations much faster than the local intrinsic relaxation times can be described via a time averaged inter-particle potential across a wide range of interaction strengths, while oscillations much slower than these relaxation times result in structures that adapt to the attraction strength of the current half-cycle. Interestingly, oscillations periods similar to these relaxation times shift the interaction window over which orderly assembly occurs by enabling error correction during the half-cycles with weaker attractions. Our results provide fundamental insights to non-equilibrium self-assembly on tem-

porally variant energy landscapes.

1 Introduction

Self-assembly is the process by which a disordered system forms ordered patterns or nanostructures without external intervention due to the interactions that are encoded within the assembling components and their environment. The driving forces behind self-assembly can organize lipids into bilayers,¹ gather capsomers into viral capsids,²⁻⁶ and arrange block copolymers into a wide range of microphase topologies.⁷

Several studies have worked to uncover governing principles that would enable the design of interparticle interactions that lead to well-ordered, self-assembled equilibrium states. As a result, we now know that the strength, placement, and specificity of the interactions between the assembling components,⁸⁻¹³ their shapes,^{8,9,12,14} and their concentrations^{5,15} can all be tuned to stabilize a specific equilibrium target structure. However, the ability to reach these equilibrium assemblies is highly dependent upon the assembly kinetics.^{5,16} Strengthening the interactions that lower the free energy of the target structure often increases the kinetic barriers to its formation, making it a challenge to design components that reliably self-

assemble on a reasonable timescale.^{10,16–18} Insightful work has been done to characterize the different dynamic pathways a system can take during self-assembly and the various types of kinetic traps that may emerge.^{18,19} One recent article has even been able to optimize interactions that not only select a target equilibrium structure, but also simultaneously control specific kinetic features along its assembly pathway.²⁰

Alternatively, dissipative self-assembly processes can result in well-ordered structures by driving a system out of equilibrium and either creating new assembly routes towards equilibrium structures or forming non-equilibrium steady-states (NESSs).^{21,22} These non-equilibrium self-assembly pathways couple an assembling system to an energy source, such as when particles are self-propelled with a constant directional force^{13,23,24} or when assembly occurs within a shear flow.^{25,26} Recently, large deviation theory has been successfully employed to optimize both interactions and external shear forces in order to target specific steady states.²⁵

The energy source in dissipative self-assembly may be temporally modulated through the change of an internal or external parameter, such as environmental changes that modify the interactions between assembling particles^{27–29} or that change their interactions with an external field.^{30–35} The self-assembly of many biological structures occurs within complex and ever-changing environments, and even certain naturally-forming non-biological materials appear to require time-variant environments to assemble – recent investigations have revealed that cycling between undersaturation and supersaturation may be necessary for the formation of naturally-occurring dolomite.^{36,37}

One way to optimize a time-dependent dissipative self-assembly pathway is to employ feedback control, in which the assembly process is monitored in real time and the driving forces are adjusted on the fly, based on that feedback, to guide the process towards a desired outcome. One such approach adjusted the inter-particle interactions during assembly simulations based on the ratio of correlation and response func-

tions and the degree to which they indicated an optimal balance of local microscopic reversibility (to avoid kinetic traps) and overall global irreversibility (towards assembly).³⁸ More generally, it has been shown that high dimensional non-equilibrium time-dependent forces are able to guide an assembly towards a desired structure, however there is an unavoidable energetic cost to doing so.³⁹ Bevan and coworkers constructed an experimental system to demonstrate the feasibility of feedback control: the 2D assembly of charged colloids were monitored in real time via optical microscopy while being subjected to a tunable electric potential. Within this set-up, the electric potential was adjusted based on feedback from the structural order parameter in order to construct perfectly crystalline configurations.^{40–42} Even so, it is clear that the need to monitor and adjust assembly conditions in real time would present significant difficulties to widely implementing feedback control approaches.

As an alternative to monitoring and adjusting each assembly process in real-time, information can be gathered from multiple simulations or experimental realizations of a dissipative assembly process and used to construct time-dependent protocols that are optimized for the ensemble of likely assembly pathways. One such approach employed evolutionary reinforcement learning to determine time-dependent temperature and chemical potential protocols for the efficient assembly of patchy disks into desired polymorphs.⁴³ Similarly, Markov state models have been constructed from simulations of colloidal oligomers and capsids in order to design optimal time-dependent interaction profiles for the finite-time folding and assembly of those systems.⁴⁴ However, significant data is required in order to optimize each time-dependent protocol, which will depend on the specifics of the system, and the implementation of these time-dependent protocols in real systems may prove challenging.

Oscillatory or cyclic changes to the environment in which assembly proceeds may provide a more experimentally accessible avenue to design new dissipative assembly pathways. A number of studies have shown that the cycli-

cal exposure of oil droplets to an external magnetic field can facilitate local relaxation processes in the resulting aggregates, thereby enabling them to overcome kinetic barriers to equilibration.^{30–35,45} In simulations of photosensitive nanoparticles, light-induced aggregation proceeded more rapidly after short pauses in the light irradiation.⁴⁶ Simulations by Risbud and Swan found that toggling inter-particle depletion interactions on and off at a timescale that allowed for sufficient particle diffusion relaxed kinetic traps and resulted in the more rapid formation of low-defect colloidal crystals.⁴⁷ Finally, joint experiment and simulation work showed that the cyclic toggling of an external electric field on a timescale close to the characteristic melting time could anneal defects in colloidal crystals.⁴⁸

Temporal environmental oscillations may also provide experimentally accessible ways to create and maintain long-lived non-equilibrium steady states (NESSs). Tagliazucchi and coworkers used simulations and theory to show that novel non-equilibrium steady state phases of binary pH-sensitive colloids can form when pH oscillations are faster than the colloid’s characteristic diffusional timescale,^{27,28} and a similar effect was observed with three dimensional close packed colloids.²⁹ Additional simulations have shown that oscillations in inter-particle interactions and external fields can result in ellipsoids adopting a non-equilibrium chiral smectic phase⁴⁹ and in the formation of non-equilibrium lamellar structures in homopolymer mixtures.⁵⁰

Prior work has focused on the assembly of extended NESS structures or the annealing of defects in extended colloidal crystals. In this work, however, we investigate the assembly of a self-limited capsid-like model with multiple inherent length scales and relaxation timescales that arise from the internal structure of the capsid building blocks. Specifically, we probe the impact of oscillatory time-dependent interactions on the assembly mechanisms over a range of oscillation timescales and amplitudes. In Section 2, we outline the coarse grained viral capsid-like model. In Section 3.1, we discuss assembly with static interactions. Then,

in Section 3.2, we perform simulations with oscillatory interactions that are faster than, slower than, or similar to inherent relaxation timescales within the model to probe their influence on assembly. Finally, in Section 3.3, we vary oscillation amplitude to investigate how these temporal oscillations can act as an error correction technique. As summarized in Section 4, we find that the inherent timescales of the model system are critical in determining the effect of fast, intermediate, and slow oscillatory interactions on the resulting assembly process.

2 Modeling

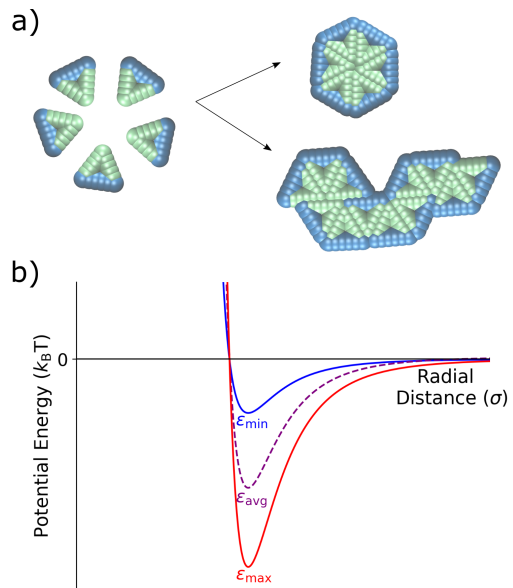


Figure 1: Schematic of the coarse-grained capsid-like model and inter-particle potential. (a) Triangular particles with two type A edges (green) and one type B edge (blue) start in a random distribution within the simulation box. Type A - type A interactions are defined via a Lennard-Jones potential, while the type A - type B and type B - type B particles interact via a Weeks-Chandler-Anderson potential.⁵¹ As the simulation proceeds, triangles can assemble into hexameric capsid-like structures or into larger snake-like aggregates. (b) The Lennard-Jones potential for the type A - type A interaction, showing the two different values of $\epsilon - \epsilon_{\min}$ and $\epsilon_{\max} -$ with the time-averaged ϵ_{avg} shown in purple.

Viral capsid models have proven essential in the theoretical and computational study of self-assembly, due in part to their organization into self-limiting ordered structures.^{5,15,19,52–59} Inspired by earlier studies on capsid assembly, in this work we investigate the assembly of two-dimensional, rigid triangular particles that assemble into capsid-like hexamers, as shown in Fig. 1a. The model was based upon a similar one in Mallory and Cacciuto’s work on the role of self-propulsion in capsid-like colloidal assembly.¹³ The placement of attractive particles (green) on only two edges of the triangles causes these monomer units to assemble either into distinct hexamers or into extended snake-like structures (see Fig. 1a).

The triangular monomers are composed of fifteen partially overlapping circular subparticles that are rigidly held together, as shown in Fig. 1a. Each subparticle is assigned one of two different types, A or B, which determines its interparticle potential. The subparticles on two edges of the equilateral triangle are assigned type A (green) and interact via a Lennard-Jones (LJ) potential, the strength of which can be tuned by changing ϵ , the LJ well-depth. The subparticles on the third edge are assigned type B (blue) and interact via the Weeks-Chandler-Anderson (WCA) potential.⁵¹ Thus, type B subparticles are purely repulsive, and interactions between type A and type B subparticles are also defined by the WCA potential. The placement of these differently-interacting subparticles introduces an overall anisotropic interaction between the individual triangular particles. Fig. 1b illustrates the attractive interactions between the type A subparticles of different triangular particles for various ϵ values. A more detailed descriptions of the particles and interactions can be found in the Supporting Information.

Oscillatory interactions are implemented by switching the ϵ value of the type A-type A interactions between ϵ_{\min} and ϵ_{\max} in a square wave pattern. We investigate the effect on capsid formation of variations in both the oscillation period and its amplitude (defined as the magnitude of the shift in each direction from the central, ϵ_{avg} -value). Variations in ϵ are con-

sidered here as a way to investigate the effects of a temporally-dependent interaction strength on assembly.

Simulations begin with a randomly distributed system of 150 triangular particles in a periodic box with no particle overlap. Langevin Dynamics is utilized to evolve the system in time, which also provides a thermostat to maintain a constant temperature over the simulation and mimics the drag and random fluctuations associated with the dynamics of solvated particles. The system is first allowed to equilibrate with the type A interactions turned off and all subparticles interacting via the WCA potential, as this ensures that there is no particle overlap while establishing a random initial distribution of the triangles, both spatially and orientationally. After the equilibration period, the Type A attractive interactions are turned on, and the system is progressed for $150,000\tau$. See Supporting Information for additional details.

3 Results and Discussion

3.1 Capsid assembly is non-monotonic with attraction strength.

We first model the formation of the complete capsid-like hexamers within a series of static environments, each with fixed effective interactions, ranging from $\epsilon = 0.75k_B T$ to $\epsilon = 2.25k_B T$. Figure 2a shows the resulting capsid yields and sample configurations as a function of ϵ for three different simulation times, and Figure 2b shows how the presence of differently-sized aggregates changes with ϵ and simulation time.

In keeping with prior work on similar models of viral capsids,^{5,13,19,53,55,57} we observe in Figure 2a that capsid assembly is non-monotonic with interaction strength. As ϵ increases from $0.75k_B T$ to $1.35k_B T$, capsid yield also increases. However, above $\epsilon = 1.35k_B T$, capsid yield decreases. This non-monotonic trend is due to a transition from thermodynamically equilibrated systems on the left-hand side of the curve to kinetically constrained systems on

the right-hand side as interactions become too strong for full equilibration to occur within the simulation time. Sampling for various lengths of time verifies this transition from thermodynamic to kinetic products, as the left-hand side of the curve remains unchanged for sampling times ranging from $75,000\tau$ to $600,000\tau$, while the right-hand side shifts to higher values as sampling times lengthen and the kinetically constrained structures have additional time to relax.

The inset snapshots in Figure 2a provide further evidence of this transition. At low ϵ interaction strengths, such as shown for $\epsilon = 0.95k_B T$, most triangles exist as free monomers or in small aggregates, and only a few complete capsids form. By $\epsilon = 1.35k_B T$, the snapshot shows almost complete capsid formation. However, at $\epsilon = 1.75k_B T$, well-formed capsids appear alongside larger, snake-like and kinetically trapped aggregates, with the number of snake-like aggregates decreasing and the number of capsids increasing as simulation times lengthen.

To better probe capsid assembly kinetics, in Figure 2b we track the percent of the triangular monomers that are assembled into differently sized aggregates as a function of simulation time. At a weaker interaction strength of $\epsilon = 0.95k_B T$, the system almost instantaneously assembles into small aggregates of 2-6 monomers (turquoise) in length, which slightly decreases over the first $1 \times 10^4\tau$ of the simulation as a small number of capsids (cyan) assemble. At an intermediate attraction strength of $\epsilon = 1.35k_B T$, a significant number of longer aggregates composed of 7-10 (purple) and 11+ (magenta) monomers rapidly form initially, but then decrease on the same timescale as capsid structures emerge. At a stronger attraction of $\epsilon = 1.75k_B T$, where the capsid yield curve has crossed into the kinetic regime, most monomers rapidly assemble into the largest aggregates (magenta), which only slightly and gradually convert into capsids over the remainder of the simulation time. By $150,000\tau$, most monomers remain in these very large aggregates due to the difficulties in overcoming the high energetic barriers associated with strong inter-particle interactions.

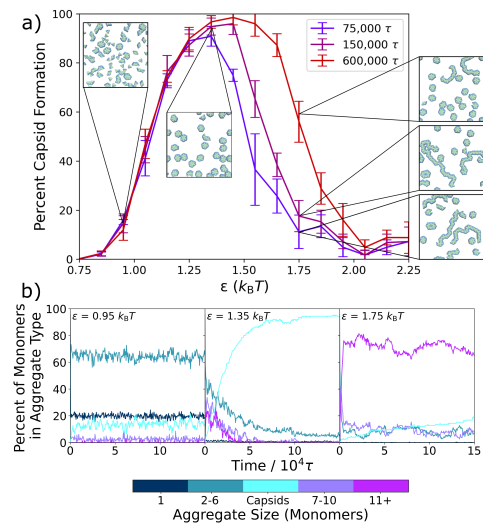


Figure 2: Capsid yield and aggregate formation within the static system. a) Capsid yield curves are plotted after three different simulation times vs. the attraction strength, ϵ . As simulation time increases, the capsid yield does not change on the left hand side of the curve. However, on the right hand side, capsid yield increases with longer simulation time. Inset are final snapshots of the system at $\epsilon = 0.95k_B T$, $\epsilon = 1.35k_B T$, and $\epsilon = 1.75k_B T$. b) The percentage of triangular monomers within each group of different sized aggregates is plotted over $150,000\tau$ for three different ϵ values ($\epsilon = 0.95k_B T$, $\epsilon = 1.35k_B T$, and $\epsilon = 1.75k_B T$). Aggregates of varying size are shown with the color bar, with the hexameric structure shown in cyan. Capsid yields and kinetic traces are averaged over five independent trajectories, and the error bars in (a) display the standard deviation.

Interestingly, at the intermediate and stronger attraction values, the assembly process in Figure 2b follows a non-classical, two-step assembly pathway.^{60,61} During non-classical assembly pathways, which have been seen in protein^{11,62,63} and colloidal particle crystallization,⁶⁴⁻⁶⁶ the system assembles into a condensed, disordered phase that has a lower free energy barrier to nucleation than the disassembled system, so that the final assembled structure grows from pre-formed aggregates.^{63,65,66} This process is clearly in evidence at both $\epsilon = 1.35k_B T$ and $\epsilon = 1.75k_B T$ in Fig-

ure 2b, where capsid counts increase as the initially assembled larger aggregates decrease. To probe exactly the ϵ values at which this changeover in assembly mechanism occurs, we expand Figure 2b in Figure S2 and plot the results for values ranging from $\epsilon = 0.75k_B T$ to $\epsilon = 2.15k_B T$ at $0.10k_B T$ intervals. Evidence for this two-step mechanism can be seen as early as $\epsilon = 1.25k_B T$, and a clear cross-over is seen around $\epsilon = 1.45k_B T$, where non-capsid monomers are present in smaller and larger aggregates in about equal numbers, with both types of aggregates decreasing as capsids form. At higher ϵ values, the two-step pathway dominates, with most monomers assembling rapidly into the larger, snake-like aggregates.

Having established the assembly behavior of the 2D model capsid system within a series of static environments, we now temporally vary the inter-monomer attractions by switching the strength of the Lennard-Jones potential between two values during assembly. We define the stronger attraction strength as ϵ_{\max} and the weaker interaction strength as ϵ_{\min} . The oscillation amplitude defines the distance of ϵ_{\max} and ϵ_{\min} from a central ϵ_{avg} value, where $\epsilon_{\text{avg}} = (\epsilon_{\max} + \epsilon_{\min})/2$. See Figure 1. We also define the period of oscillation, τ_{osc} , as the time it takes to complete a full cycle, with half the cycle at ϵ_{\max} and the other half at ϵ_{\min} . In the rest of the paper, we investigate how these oscillatory interactions influence capsid formation across a variety of oscillation periods (Sections 3.2) and oscillation amplitudes (Section 3.3).

3.2 Assembly depends on the oscillation frequency.

First, we consider how different oscillation periods, τ_{osc} , affect the assembly process. During the ϵ_{\max} half-cycle, triangular monomers are more strongly attractive and assemble together, while in the ϵ_{\min} half-cycle, such structures may rearrange or be broken apart. The degree to which assembly and disassembly occurs depends upon the time spent in each half-cycle, and how that time compares to the time required for the system to equilibrate.

Previous studies investigating oscillations in

inter-colloidal potentials compare τ_{osc} to a characteristic diffusional time-scale, $t_d = \sigma^2/D$, where σ specifies the size of the assembling colloids and D is the diffusion coefficient.^{27,47} Oscillation periods that are significantly shorter than the characteristic diffusional time-scale ($\tau_{\text{osc}} \ll t_d$) are considered to be at the fast oscillation limit, while at the slow oscillation limit, periods are long enough to allow the system to relax to different equilibrium structures during each oscillation half-cycle.^{27,28,47}

As can be seen in the structure shown in Figure 1, more than one length-scale is needed to fully describe the assembling particles; the diameter of the circular subparticles is $\sigma_{\text{LJ}} = 0.25\sigma$, while the edge length of the triangular particles is 1σ . In addition, at the higher attraction strengths we probe, capsid formation proceeds via the initial formation of a condensed disordered phase (see Fig. 2a) and its subsequent relaxation. The multiple length-scales and assembly pathways within this model are expected to influence how capsid formation varies with oscillation frequency.

To better understand the interplay of the oscillation period and these inherent length-scales, we list in Table 1 a set of key distances that characterize important energetic and structural changes, ranging from the distance required to reduce the attractive interaction to a tenth of its maximum strength to the full edge length of a single triangular particle. To estimate how long it would take for the triangular particles to traverse these distances, we plot the mean squared displacement vs. time for a single triangular particle in Figure S3a. Since the relevant length scales span the ballistic and diffusive time regimes, we estimate the time it takes for the particle to move over these critical distances directly from the results in Figure S3a. Additionally, we plot in Figure S3b the rotational autocorrelation function vs. time for a single triangular particle and calculate the mean rotational lifetime using an exponential decay fit. Below, we first consider oscillations at the fast limit, where the period is shorter than the timescales associated with these key distances ($\tau_{\text{osc}} \ll \{t_d\}$), and show that the assembly behavior in this regime

can be described by the ϵ value averaged over a single oscillation period, ϵ_{avg} . Next, we investigate slow oscillations, where the period is longer than the timescales that correspond to the distances in Table 1 ($\tau_{\text{osc}} \gg \{t_d\}$), such that the system has time to at least partially equilibrate to the current ϵ value during each half period of the oscillation. Lastly, we simulate oscillations in the intermediate regime ($\tau_{\text{osc}} \approx \{t_d\}$) and show how the window of capsid assembly shifts with the oscillation period.

Table 1: Characteristic lengths and their corresponding relaxation times. Important length-scales within the model are provided along with the estimated time, t_d , that it takes for a single, isolated, triangle particle to move over that distance or to lose its rotational orientation, based on its mean squared displacement and its rotational autocorrelation function (see Figure S3).

Characteristic Distance	Distance (σ)	t_d (τ)
$0.72\sigma_{\text{LJ}} (-\epsilon \rightarrow -0.1\epsilon)$	0.18	0.59
Diameter of Subparticle	0.25	0.91
Edge of Triangle	1.00	10.33
Rotational Relaxation ³	–	7.10

³For the rotational relaxation, t_d describes the mean lifetime for the exponential decay from the rotational correlation function in Figure S3b.

The fast oscillation limit obtains the equilibrium yield curve for a well-depth of ϵ_{avg} . In prior work on colloidal assembly under an oscillatory potential, Szleifer and coworkers employed the Fokker-Planck equation while dividing up the oscillation period into a series of infinitesimally small time steps to show that, when the period of oscillation is much, much shorter than the inherent diffusional time-scale of the simulated colloidal particles, the oscillatory interaction potential can be described by a static effective inter-particle potential that is equal to the time-averaged potential over a single oscillation period.^{27,28} In our system, where we oscillate the well-depth of the Lennard-Jones potential such that half of each oscillation period is at a strength of ϵ_{max} and half at a strength of ϵ_{min} , the time-averaged potential over a single period works

out to be the LJ potential with a well depth of $\epsilon_{\text{avg}} = (\epsilon_{\text{max}} + \epsilon_{\text{min}})/2$ (see SI for details).

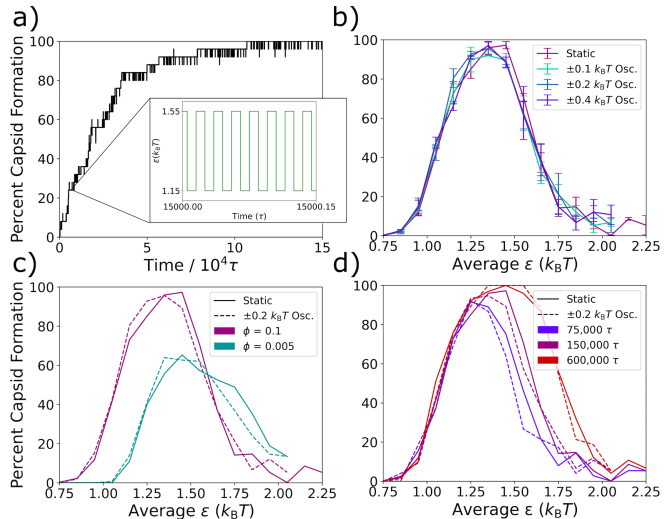


Figure 3: Assembly at the fast oscillation limit. (a) A kinetic trace is shown from a single $150,000\tau$ trajectory of the assembling capsids at an attraction strength of $\epsilon_{\text{avg}} = 1.35k_B T$, an oscillation amplitude of $0.2k_B T$, and an oscillation period of 0.02τ . Inset displays a zoomed in schematic of the oscillation waveform to compare the oscillation frequency to the timescale of capsid assembly. (b) Capsid yield curves at $150,000\tau$ are plotted for three different amplitudes as well as the non-oscillatory system at a period of 0.02τ . (c) Capsid yield curves at $150,000\tau$ are plotted for the oscillatory system at a period of 0.02τ and the static potential are shown at two different densities. (d) Capsid yield curves at three different simulation times are plotted for the static system (solid lines) and compared to the results for the system with interactions oscillated for a period of 0.02τ with an amplitude of $0.2k_B T$ (dashed lines). Percent capsid formation is averaged over three independent trajectories, and the average standard deviations for the capsid yield measurements were $\pm 3.2\%$ for the static systems and $\pm 3.8\%$ for the oscillatory systems.

To test the the behavior of our system at the fast oscillation limit, in Figure 3 we compare the degree of capsid formation at static ϵ values to that at the corresponding ϵ_{avg} values for various oscillation amplitudes, monomer concentrations, and simulation times. An oscillation

period of 0.02τ was chosen (see Fig. 3a), which is expected to yield fast limit behavior since it is much shorter than the calculated time-scales of interest in Table 1. In Figure 3b, we confirm that this period reproduces the static non-monotonic yield curve across three different oscillation amplitudes. In Figure 3c, we test the correspondence between the static and effective potentials across changes in particle density. The static yield curves (solid lines) at volume fractions of $\phi = 0.1$ and $\phi = 0.005$ differ, which is expected since a decreased volume fraction requires a stronger ϵ for capsid formation. However, at both densities, the oscillatory potential with a period of 0.02τ and an amplitude of $0.2k_B T$ (dashed lines) returns the corresponding static yield curve for ϵ_{avg} . Finally, in Figure 3d, we investigate the timescales of relaxation at the fast oscillation limit as compared to those in the static system by comparing the oscillatory and static capsid yield curves after simulation times of $75,000\tau$, $150,000\tau$, and $600,000\tau$. We find that capsid formation at the fast oscillation limit increases with simulation time in precisely the same way as capsid formation does within the corresponding static potential. This result suggests that kinetic traps affect the system dynamics at the fast oscillation limit in the same way as in the static system, supporting the prior claim that even a system's non-equilibrium dynamics can be described by an appropriate time-averaged potential at the fast oscillation limit²⁸ and explaining the observation that in both Fig. 3b and Fig. 3c, the correspondence between the oscillatory and static curves is as good for the kinetically constrained right-hand side of the curve as it is for the thermodynamically equilibrated left-hand side. In summary, when the Lennard-Jones potential is oscillated at a very short period of 0.02τ , the system organizes in the same manner as with the non-oscillatory potential across a number of tested variations.

Under slow oscillations, the system adapts to the ϵ value of each half-cycle. Next we look at the slow oscillation limit, where the period is longer than the displacement times $\{t_d\}$ in Table 1, and the system has sufficient time within a single half-cycle to adapt itself

substantially to the current ϵ value. Figure 4 plots capsid yield as a function of simulation time for the static reference case (a) and three longer oscillation periods (b-d), for three different ϵ_{avg} values, all with an oscillation amplitude of $0.4k_B T$.

In the Figure 4a static case, a weaker attraction strength of $\epsilon_{\text{avg}} = 1.05k_B T$ results in the capsid yield quickly plateauing to about 40%, a moderate attraction strength of $\epsilon_{\text{avg}} = 1.35k_B T$ results in nearly complete capsid assembly over a slightly longer time-scale, and a stronger interaction strength of $\epsilon_{\text{avg}} = 1.65k_B T$ results in kinetic trapping and slow capsid assembly.

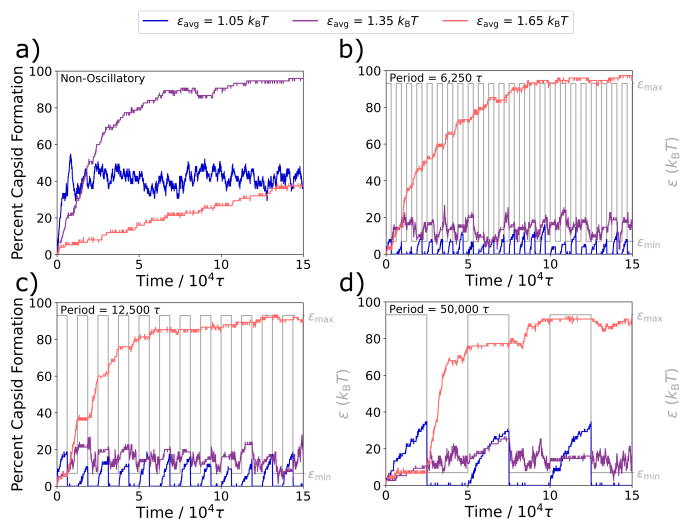


Figure 4: Capsid formation changes with each half-cycle. Capsid formations at different ϵ_{avg} values are shown at an oscillation amplitude of $0.4k_B T$ for three longer periods, as compared to the non-oscillatory capsid formation curves in (a). We show (b) $\tau_{\text{osc}} = 6,250\tau$, (c) $\tau_{\text{osc}} = 12,500\tau$, and (d) $\tau_{\text{osc}} = 50,000\tau$. Each period has the waveform overlaid in gray to show the oscillation period. The kinetic traces are averaged over three independent trajectories.

In Figure 4b-d, we plot capsid formation along with the oscillation profiles for periods of $6,250\tau$, $12,500\tau$, and $50,000\tau$, where $\tau_{\text{osc}} \gg \{t_d\}$. For the weakest interaction strength of $\epsilon_{\text{avg}} = 1.05k_B T$ (in blue), at the given amplitude of $0.4k_B T$, the simulation oscillates between a well-depth of $\epsilon_{\text{min}} = 0.65k_B T$ and $\epsilon_{\text{max}} = 1.45k_B T$. For all three τ_{osc} periods, cap-

sids rapidly assemble in the ϵ_{\max} half-cycle and rapidly disassemble in the ϵ_{\min} half-cycle, where interactions are too weak for the structures to remain intact. As with the weakest ϵ_{avg} value, simulations at the strongest ϵ_{avg} value investigated here of $1.65 k_B T$ (in orange) also display significantly different assembly behaviors in each half-cycle. At these stronger attraction strengths, capsids no longer rapidly fall apart during the ϵ_{\min} half-cycles, however the kinetically trapped snake-like structures can still relax to form additional capsids. As a result, significant capsid formation occurs during the ϵ_{\min} half-cycles of $\epsilon_{\text{avg}} = 1.65 k_B T$. These capsids remain intact during the ϵ_{\max} half-cycles, however the stronger attractive forces keeping the subparticles together also largely arrest the relaxation of kinetic traps and thus the formation of additional capsids. Behavior with the intermediate ϵ_{avg} of $1.35 k_B T$ (in purple) is more complex. The system oscillates between $\epsilon_{\min} = 0.95 k_B T$ and $\epsilon_{\max} = 1.75 k_B T$, both of which result in only modest capsid yields in the static system (see Figure 2a), and we observe that same modest yield in all three longer oscillation periods in Fig. 4b-d, despite the fact that a high yield is obtained for $\epsilon = 1.35 k_B T$ in the static case in Fig. 4a.

Overall, when considering oscillations that are slow compared to the characteristic displacement times in Table 1, we see that the system substantially adapts to each half-cycle, which can result in capsid yields that grow and shrink over each oscillation or in capsid yields that remain static during most ϵ_{\max} half-cycles and then further increase during most ϵ_{\min} half-cycle. It is important to note that even the very long oscillation periods investigated here are still slower than the time needed to fully relax the kinetic traps of the system, which can take longer than $75,000\tau$ even at $\epsilon = 1.45 k_B T$, just slightly above the capsid yield curve’s peak (see Fig.2a).

Intermediate oscillation periods causes yield curves to shift to stronger ϵ_{avg} -values. In order to probe how oscillatory interactions influence capsid assembly between the fast and slow oscillation limits, in Figure 5 we plot the capsid yield curves across a range of

oscillation periods at an amplitude of $0.4k_B T$. Details of aggregate formation for three of these periods are shown for a range of ϵ_{avg} values in Figure S4.

For all periods, capsid assembly remains non-monotonic with interaction strength, and the window of orderly assembly is approximately the same width for systems undergoing oscillatory interactions as for those with static interactions. However, as the period of oscillation increases in Figure 5a, the capsid yield curves shift to higher ϵ_{avg} values.

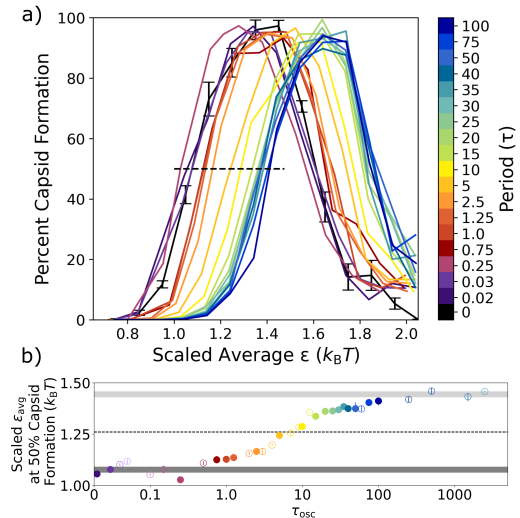


Figure 5: Capsid yield curves for different periods of oscillation. (a) Capsid yield curves after $150,000\tau$ are compared to the scaled ϵ_{avg} value for different oscillation periods at an amplitude of $0.4k_B T$. The black, dashed line indicates 50% capsid formation on the left hand side of the yield curves. (b) The scaled ϵ_{avg} values that result in 50% capsid formation on the left hand side of the capsid yield curve are plotted vs. τ_{osc} . The dark gray bar indicates the non-oscillatory regime, the light gray bar plots the upper asymptotic limit of a sigmoidal fit, and the dotted line indicates the midpoint between the two. Points in (b) that are shown in (a) are represented by a closed circle, while additional periods not shown in (a) are denoted by an open circle. Capsid formation is averaged over three independent trajectories, and the error bars on the static curve show its standard deviation.

One technical complication that arises as the

oscillation period increases slightly from the fast oscillation limit period of 0.02τ is that the Langevin thermostat is not able to generate the target temperature from about 0.03τ to about 5τ . To enable comparisons that include these oscillation frequencies, the ϵ_{avg} values in Figure 5 were therefore scaled appropriately for the actual observed temperature at each oscillation period. A plot of these temperatures vs. oscillation period is shown in Figure S1 in the SI, and additional details on the scaling can be found there as well.

To quantify the capsid yield curve shift, in Figure 5b we plot the scaled ϵ_{avg} value that results in 50% capsid formation on the left hand side of the yield curves in Fig. 5a (i.e., where it intersects the black dashed line) vs. the oscillation period, τ_{osc} . The ϵ value that results in 50% capsid formation in the static system is indicated by the dark gray bar, while the corresponding ϵ_{avg} value for the long oscillation periods is indicated by the light grey bar.

The result for the fast oscillation limit ($\tau_{\text{osc}} = 0.02\tau$) overlaps with the non-oscillatory dark gray bar, as previously observed in Fig. 3. For oscillation periods between 0.02τ and about 0.5τ , the scaled ϵ_{avg} values are clustered around the dark gray bar and there is no sustained shift away from the static ϵ value. After 0.5τ , however, the scaled ϵ_{avg} value at 50% capsid formation steadily increases with oscillation period, crosses the dotted line that indicates the halfway point between the fast and slow oscillation limits at a period of about $\tau_{\text{osc}} = 7\tau$, and then plateaus at the slow oscillation value (light grey bar).

To make sense of the shift with oscillation period in Fig. 5, we return to the inherent length-scales of our model and their corresponding local relaxation time-scales, as described in Table 1. After aggregates nucleate, there are three important local relaxation processes that facilitate the second stage of the hexagonal capsid formation from either smaller or larger aggregates: (1) the diffusion of subparticles away from one another; (2) the sliding of triangular particle edges along one another; and (3) the rotation of a triangular particle away from or towards another. All three of these move-

ments are more likely to occur during the ϵ_{min} half-cycle when attractions are weaker. Table 1 provides estimates for the timescales of these local relaxation processes, based on simulations of a single triangular particle (see Figure S3). First, the diffusion of one subparticle out of the LJ attractive well of a neighboring subparticle is characterized by the length-scale of the LJ attraction. The distance a subparticle must move for the attractive interaction to be reduced to a tenth of its full strength is 0.18σ , which is estimated to take approximately 0.6τ . Second, the edge length of a single triangular particle is 1.0σ , and the corresponding diffusion time for that distance is 10.3τ . Third, the mean lifetime for the rotational degree of freedom is estimated to be 7.1τ , based on the rotational correlation function calculated in Figure S3. These intrinsic local relaxation timescales aid our interpretation of the shift in the capsid yield curves with oscillation period in Fig. 5.

At a period of $\tau_{\text{osc}} = 0.5\tau$, where the steady shift towards higher ϵ_{avg} values starts, there is just enough time during each ϵ_{min} half-period for a subparticle to move away from a neighbor so that their attractive LJ interaction is reduced by two thirds. At a period of about 1.2τ , the ϵ_{min} half-cycle is just slightly longer than the time it takes for a subparticle's LJ interaction to be reduced to a tenth of its maximum strength, on average. That is, particles that were originally interacting are likely to diffuse far enough from their original configurations so that they no longer experience a significant attraction to their original neighbors.

The black dashed line indicates the half-way mark between the fast and slow oscillation behaviors, which happens at an oscillation period of about $\tau_{\text{osc}} = 7\tau$. From Table 1, we see that several local relaxation processes that are helpful in the formation of capsids are achievable within an ϵ_{min} half-period of 3.5τ . Within this half-cycle, particles can diffuse far enough from their original configurations so that they no longer experience a significant attraction to their original neighbors, even shifting the full diameter of a subparticle. If a particle located in an aggregate can shift a subparticle away from their original configuration, this

could lower the energetic barrier for the triangle to diffuse from an aggregate structure.

After a period of 20τ , we observe the start of a plateau in the scaled ϵ_{avg} values that corresponds to 50% capsid formation. Interestingly, a period of 20τ corresponds to a half-cycle of 10τ , which is about the time needed for a triangular particle to diffuse 1σ , or the distance of one full edge of the triangle. This edge length is an important distance in disrupting longer aggregates, since a particle in the middle of a snake-like aggregate would need to diffuse about 1σ to leave the aggregate and thereby break up a longer aggregate. In addition, this length is central to the motions of a trimer of particles that enable full capsid formation from a half-capsid structure on the end of a snake-like aggregate, as can be seen in Figure 1. Given the mean rotational lifetime of approximately 7τ , it is clear that by an oscillation period of 20τ , triangular particles can fully diffuse from aggregate structures and rotate to better align with other particles to facilitate capsid formation during the ϵ_{min} half-cycles.

3.3 Shift in capsid yield with amplitude provides evidence for the critical role of error correction.

Previously, Risbud and Swan⁴⁷ and others^{30–35,45} observed that oscillating attractions could result in local relaxation, since the system was able to relax kinetic barriers via diffusion when the attractions were turned off. In our model, the formation of capsid-like structures is also limited by kinetic traps at stronger attractions, as demonstrated in Figure 2a by the increase in capsid yield with longer simulation times. In addition, at these higher ϵ values, the initial formation of snake-like structures that can convert into capsid-like hexamers makes it clear that error correction – the ability of sub-optimally assembled particles to rearrange themselves into a more favorable structure – plays an important role in the total capsid yield, both in the static and oscillatory interaction cases. Indeed, in Figure 4b-d, at

the slow oscillation limit with an amplitude of $0.4k_{\text{B}}T$, we directly observed the effect of error correction on the capsid formation process during the lower ϵ_{min} half-cycles for the case where $\epsilon_{\text{avg}} = 1.65k_{\text{B}}T$. Capsid yields almost always remained static in the ϵ_{max} half-cycles, but ratcheted up to higher levels in the ϵ_{min} half-cycles. In this section, we further probe how the ϵ_{min} half-cycles affect error correction within this model system by varying the oscillation amplitude. As the amplitude increases, ϵ_{avg} stays the same, but attractions oscillate between a weaker ϵ_{min} and stronger ϵ_{max} . Results are shown in Figure 6 for an intermediate oscillation period of 100τ , which is long enough for most local relaxation processes to occur – see Table 1 and the almost-completed shift towards the long-time oscillation value at 100τ in Figure 5b.

In Figure 6a, we show a series of capsid yield curves at different oscillation amplitudes plotted vs. ϵ_{avg} . As amplitude increases, yield curves shift to the right to higher ϵ_{avg} values – values where orderly assembly is not observed in the static system. However, when we plot these same yield curves vs. ϵ_{min} instead of ϵ_{avg} in Figure 6b, the curves for all amplitudes collapse into one curve, which is very close to the capsid yield curve for the static potential. This collapse of the yield curves indicates that, at oscillation periods sufficiently longer than the local intrinsic relaxation processes in the system, the main determinant of capsid yield in the oscillatory system is simply the value of ϵ_{min} . Indeed, this full shift from the yields observed at ϵ_{avg} to those observed at ϵ_{min} as the oscillation periods lengthen can be clearly seen in Figure 5.

To further probe this shift to the ϵ_{min} value fully determining the yield at oscillation times longer than the local relaxation processes, in Figure 6c we show the percent of the triangular monomers in each aggregate size as a function of time for a series of simulations with varying amplitudes and ϵ_{min} values. From the top row to the bottom row, ϵ_{min} increases, while within each row, ϵ_{min} is held fixed while the amplitude increases from left to right. Notably, we find that the kinetic assembly traces for a given ϵ_{min} value are essentially the same across the three

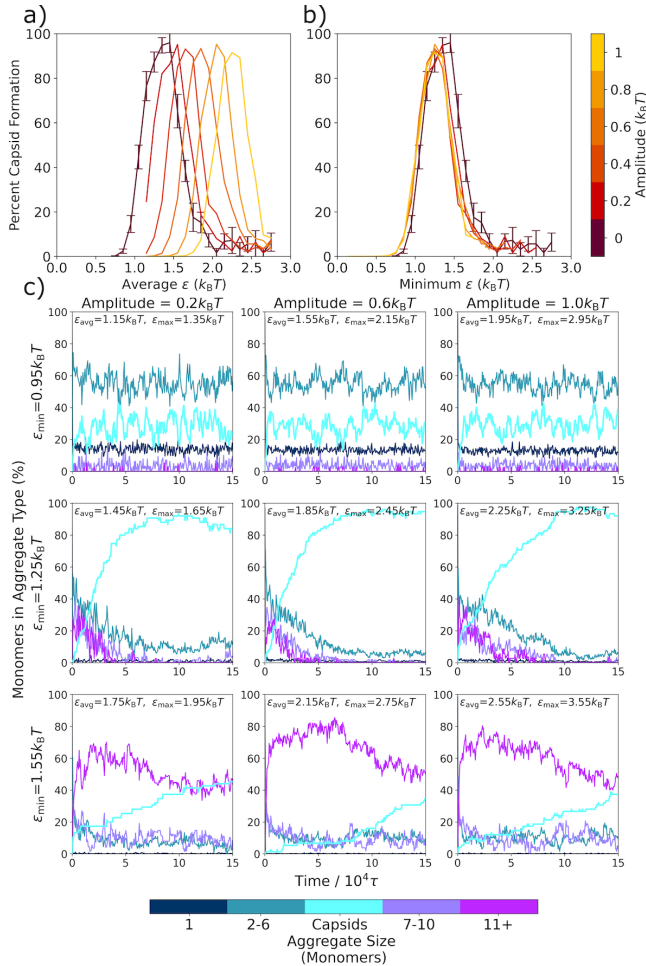


Figure 6: Capsid yield and aggregate formation for different oscillation amplitudes. Capsid yield curves are plotted in (a) vs. ϵ_{avg} and in (b) vs. ϵ_{min} for five different oscillation amplitudes with an oscillation period of 100τ and the static potential case. The formation of different sized aggregates is plotted vs. time in (c) for three different amplitudes at a period of 100τ . Although they have different ϵ_{avg} values, $\epsilon_{\text{min}} = 0.95k_B T$ for all amplitudes in row 1, $\epsilon_{\text{min}} = 1.25k_B T$ for all amplitudes in row 2, and $\epsilon_{\text{min}} = 1.55k_B T$ for all amplitudes in row 3. Capsid yield curves and monomer counts in the different aggregate types are averaged over five independent trajectories. In the static case, the error bars represent the standard deviation.

amplitudes. This result supports our finding that, as long as oscillation periods are longer than the local intrinsic relaxation processes and ϵ_{max} is above the threshold for kinetic trap formation, the strength of ϵ_{min} is what determines the degree to which kinetically trapped aggre-

gates are able to relax into fully formed capsids.

4 Conclusion

In this work, we have expanded upon previous studies to investigate how temporal oscillations influence the dissipative self-assembly of anisotropic 2D triangular particles that assemble into capsid-like structures. At stronger attractions, the formation of these hexamers occurs through a non-classical, two-step nucleation pathway and is prone to kinetic trapping, resulting in a non-monotonic dependence of capsid yield on attraction strength in both the static and oscillatory cases.

Our results highlight the correspondence between the different oscillation time-scales and the particle motions, both translational and rotational, that govern local relaxation processes. At the limit of oscillations that are very fast compared to these intrinsic time-scales, assembly proceeds as if the system were subject to the static attraction that is the time-averaged strength over a single oscillation period, defined by the averaged LJ well-depth, ϵ_{avg} . At the slow oscillation limit, the system evolves according to the attractive forces at play within the current half-cycle. In between these extremes, the assembly yield curve shifts from one determined by ϵ_{avg} to one determined by ϵ_{min} , the attraction strength during the weaker attraction half-cycles, since it is the error correction made possible at those times that determines the degree to which kinetic traps can be overcome.

Temporal oscillations in inter-particle attractions may offer experimentally accessible dissipative self-assembly protocols for a wide range of materials. Such oscillations could be implemented by changes in temperature, external applied fields, light irradiation, pH changes, or other mechanisms. Our results provide insights that could aid in the design of such protocols. Specifically, even without closed feedback loops or detailed simulations of the specific system of interest, designing protocols with interactions that oscillate over times similar to the intrinsic relaxation times of that material may be used to relax kinetically trapped structures, so long as

the attractions between the particles are weak enough at times to allow those relaxation processes to proceed and thereby facilitate error correction within an assembling material.

Author Contributions

Jessica K. Niblo: conceptualization, investigation, methodology, data curation, software, formal analysis, visualization, writing – original draft. Jacob R. Swartley: methodology, writing – reviewing. Zhongmin Zhang: methodology, writing – reviewing. Kateri H. DuBay: conceptualization, methodology, supervision, formal analysis, writing – original draft.

Conflicts of interest

There are no conflicts to declare.

Acknowledgements

This material is based upon work supported by a startup grant from the University of Virginia. The authors also acknowledge Research Computing at the University of Virginia (<https://rc.virginia.edu>) for providing computational resources and technical support.

References

- (1) Cho, N.-J.; Hwang, L. Y.; Solandt, J. J. R.; Frank, C. W. Comparison of Extruded and Sonicated Vesicles for Planar Bilayer Self-Assembly. *Materials* **2013**, *6*, 3294–3308.
- (2) Zlotnick, A. To Build a Virus Capsid : An Equilibrium Model of the Self Assembly of Polyhedral Protein Complexes. *The Journal of Molecular Biology* **1994**, *241*, 59–67.
- (3) Zlotnick, A.; Aldrich, R.; Johnson, J. M.; Ceres, P.; Young, M. J. Mechanism of Capsid Assembly for an Icosahedral Plant Virus. *Virology* **2000**, *277*, 450–456.
- (4) Hicks, S. D.; Henley, C. L. Irreversible Growth Model for Virus Capsid Assembly. *Physical Review E* **2006**, *74*, 031912.
- (5) Hagan, M. F.; Chandler, D. Dynamic Pathways for Viral Capsid Assembly. *Biophysical Journal* **2006**, *91*, 42–54.
- (6) Sigl, C.; Willner, E. M.; Engelen, W.; Kretzmann, J. A.; Sachenbacher, K.; Liedl, A.; Kolbe, F.; Wilsch, F.; Aghvami, S. A.; Protzer, U.; Hagan, M. F.; Fraden, S.; Dietz, H. Programmable Icosahedral Shell System for Virus Trapping. *Nature Materials* **2021**, *20*, 1281–1289.
- (7) Lynd, N. A.; Meuler, A. J.; Hillmyer, M. A. Polydispersity and Block Copolymer Self-Assembly. *Progress in Polymer Science* **2008**, *33*, 875–893.
- (8) Zhang, Z.; Glotzer, S. C. Self-Assembly of Patchy Particles. *Nano Letters* **2004**, *4*, 1407–1413.
- (9) Glotzer, S. C.; Solomon, M. J. Anisotropy of Building Blocks and Their Assembly into Complex Structures. *Nature Materials* **2007**, *6*, 557–562.
- (10) Hormoz, S.; Brenner, M. P. Design Principles for Self-Assembly with Short-Range Interactions. *Proceedings of the National Academy of Sciences* **2011**, *108*, 5193–5198.
- (11) Haxton, T. K.; Whitlam, S. Design Rules for the Self-Assembly of a Protein Crystal. *Soft Matter* **2012**, *8*, 3558.
- (12) Grünwald, M.; Geissler, P. L. Patterns without Patches: Hierarchical Self-Assembly of Complex Structures from Simple Building Blocks. *ACS Nano* **2014**, *8*, 5891–5897.
- (13) Mallory, S. A.; Cacciuto, A. Activity-Assisted Self-Assembly of Colloidal Particles. *Physical Review E* **2016**, *94*, 022607.
- (14) Damasceno, P. F.; Engel, M.; Glotzer, S. C. Predictive Self-Assembly of Polyhedra into Complex Structures. *Science* **2012**, *337*, 453–457.
- (15) Hagan, M. F.; Elrad, O. M. Understanding the Concentration Dependence of Viral Capsid Assembly Kinetics—the Origin of the Lag Time and Identifying the Critical Nucleus Size. *Biophysical Journal* **2010**, *98*, 1065–1074.
- (16) Grant, J.; Jack, R. L.; Whitlam, S. Analyzing Mechanisms and Microscopic Reversibility of Self-Assembly. *The Journal of Chemical Physics* **2011**, *135*, 214505.
- (17) Pawar, A. B.; Kretzschmar, I. Fabrication, Assembly, and Application of Patchy Particles. *Macromolecular Rapid Communications* **2010**, *31*, 150–168.
- (18) Whitlam, S.; Jack, R. L. The Statistical Mechanics of Dynamic Pathways to Self-Assembly. *Annual Review of Physical Chemistry* **2015**, *66*, 143–163.
- (19) Hagan, M. F.; Elrad, O. M.; Jack, R. L. Mechanisms of Kinetic Trapping in Self-Assembly and Phase Transformation. *The Journal of Chemical Physics* **2011**, *135*, 104115.
- (20) Goodrich, C. P.; King, E. M.; Schoenholz, S. S.; Cubuk, E. D.; Brenner, M. P.

- Designing Self-Assembling Kinetics with Differentiable Statistical Physics Models. *Proceedings of the National Academy of Sciences of the United States of America* **2021**, *118*, e2024083118.
- (21) Whitesides, G. M.; Boncheva, M. Beyond Molecules: Self-assembly of Mesoscopic and Macroscopic Components. *Proceedings of the National Academy of Sciences* **2002**, *99*, 4769–4774.
- (22) Fialkowski, M.; Bishop, K. J. M.; Klajn, R.; Smoukov, S. K.; Campbell, C. J.; Grzybowski, B. A. Principles and Implementations of Dissipative (Dynamic) Self-Assembly. *The Journal of Physical Chemistry B* **2006**, *110*, 2482–2496.
- (23) Ilse, S. E.; Holm, C.; de Graaf, J. Surface Roughness Stabilizes the Clustering of Self-Propelled Triangles. *The Journal of Chemical Physics* **2016**, *145*, 134904.
- (24) Löwen, H. Active Colloidal Molecules. *Europhysics Letters* **2018**, *121*, 58001.
- (25) Das, A.; Limmer, D. T. Variational Design Principles for Nonequilibrium Colloidal Assembly. *The Journal of Chemical Physics* **2021**, *154*, 014107.
- (26) Das, A.; Limmer, D. T. Nonequilibrium Design Strategies for Functional Colloidal Assemblies. *Proceedings of the National Academy of Sciences* **2023**, *120*, e2217242120.
- (27) Tagliazucchi, M.; Weiss, E. A.; Szleifer, I. Dissipative Self-Assembly of Particles Interacting through Time-Oscillatory Potentials. *Proceedings of the National Academy of Sciences* **2014**, *111*, 9751–9756.
- (28) Tagliazucchi, M.; Szleifer, I. Dynamics of Dissipative Self-Assembly of Particles Interacting through Oscillatory Forces. *Faraday Discussions* **2016**, *186*, 399–418.
- (29) Long, C.; Lei, Q.-l.; Ren, C.-l.; Ma, Y.-q. Three-Dimensional Non-Close-Packed Structures of Oppositely Charged Colloids Driven by pH Oscillation. *The Journal of Physical Chemistry B* **2018**, *122*, 3196–3201.
- (30) Promislow, J. H. E.; Gast, A. P. Magnetorheological Fluid Structure in a Pulsed Magnetic Field. *Langmuir* **1996**, *12*, 4095–4102.
- (31) Promislow, J. H. E.; Gast, A. P. Low-Energy Suspension Structure of a Magnetorheological Fluid. *Physical Review E* **1997**, *56*, 642–651.
- (32) Swan, J. W.; Vasquez, P. A.; Whitson, P. A.; Fincke, E. M.; Wakata, K.; Magnus, S. H.; De Winne, F.; Barratt, M. R.; Agui, J. H.; Green, R. D.; Hall, N. R.; Bohman, D. Y.; Bunnell, C. T.; Gast, A. P.; Furst, E. M. Multi-Scale Kinetics of a Field-Directed Colloidal Phase Transition. *Proceedings of the National Academy of Sciences* **2012**, *109*, 16023–16028.
- (33) Swan, J. W.; Bauer, J. L.; Liu, Y.; Furst, E. M. Directed Colloidal Self-Assembly in Toggled Magnetic Fields. *Soft Matter* **2014**, *10*, 1102–1109.
- (34) Bauer, J. L.; Liu, Y.; Kurian, M. J.; Swan, J. W.; Furst, E. M. Coarsening Mechanics of a Colloidal Suspension in Toggled Fields. *The Journal of Chemical Physics* **2015**, *143*, 074901.
- (35) Kim, H.; Sau, M.; Furst, E. M. An Expanded State Diagram for the Directed Self-Assembly of Colloidal Suspensions in Toggled Fields. *Langmuir* **2020**, *36*, 9926–9934.
- (36) García-Ruiz, J. M. A Fluctuating Solution to the Dolomite Problem. *Science* **2023**, *382*, 883–884.
- (37) Kim, J.; Kimura, Y.; Puchala, B.; Yamazaki, T.; Becker, U.; Sun, W. Dissolution Enables Dolomite Crystal Growth

- near Ambient Conditions. *Science* **2023**, *382*, 915–920.
- (38) Klotsa, D.; Jack, R. L. Controlling Crystal Self-Assembly Using a Real-Time Feedback Scheme. *The Journal of Chemical Physics* **2013**, *138*, 094502.
- (39) Chennakesavalu, S.; Rotskoff, G. M. Probing the Theoretical and Computational Limits of Dissipative Design. *The Journal of Chemical Physics* **2021**, *155*, 194114.
- (40) Juárez, J. J.; Bevan, M. A. Feedback Controlled Colloidal Self-Assembly. *Advanced Functional Materials* **2012**, *22*, 3833–3839.
- (41) Xue, Y.; Beltran-Villegas, D. J.; Tang, X.; Bevan, M. A.; Grover, M. A. Optimal Design of a Colloidal Self-Assembly Process. *IEEE Transactions on Control Systems Technology* **2014**, *22*, 1956–1963.
- (42) Tang, X.; Rupp, B.; Yang, Y.; Edwards, T. D.; Grover, M. A.; Bevan, M. A. Optimal Feedback Controlled Assembly of Perfect Crystals. *ACS Nano* **2016**, *10*, 6791–6798.
- (43) Whitelam, S.; Tamblyn, I. Learning to Grow: Control of Material Self-Assembly Using Evolutionary Reinforcement Learning. *Physical Review E* **2020**, *101*, 052604.
- (44) Trubiano, A.; Hagan, M. F. Optimization of Non-Equilibrium Self-Assembly Protocols Using Markov State Models. *The Journal of Chemical Physics* **2022**, *157*, 244901.
- (45) Martín-Roca, J.; Horcajo-Fernández, M.; Valeriani, C.; Gámez, F.; Martínez-Pedrero, F. Field-Pulse-Induced Annealing of 2D Colloidal Polycrystals. *Nanomaterials* **2023**, *13*, 397.
- (46) Jha, P. K.; Kuzovkov, V.; Grzybowski, B. A.; Olvera de la Cruz, M. Dynamic Self-Assembly of Photo-Switchable Nanoparticles. *Soft Matter* **2012**, *8*, 227–234.
- (47) Risbud, S. R.; Swan, J. W. Dynamic Self-Assembly of Colloids through Periodic Variation of Inter-Particle Potentials. *Soft Matter* **2015**, *11*, 3232–3240.
- (48) Kao, P.-K.; VanSaders, B. J.; Glotzer, S. C.; Solomon, M. J. Accelerated Annealing of Colloidal Crystal Monolayers by Means of Cyclically Applied Electric Fields. *Scientific Reports* **2021**, *11*, 11042.
- (49) Chen, Z.-Q.; Sun, Y.-W.; Zhu, Y.-L.; Li, Z.-W.; Sun, Z.-Y. A Chiral Smectic Phase Induced by an Alternating External Field. *Soft Matter* **2022**, *18*, 2569–2576.
- (50) Pigard, L.; Müller, M. Interface Repulsion and Lamellar Structures in Thin Films of Homopolymer Blends Due to Thermal Oscillations. *Physical Review Letters* **2019**, *122*, 237801.
- (51) Weeks, J. D.; Chandler, D.; Andersen, H. C. Role of Repulsive Forces in Determining the Equilibrium Structure of Simple Liquids. *The Journal of Chemical Physics* **1971**, *54*, 5237–5247.
- (52) Jack, R. L.; Hagan, M. F.; Chandler, D. Fluctuation-Dissipation Ratios in the Dynamics of Self-Assembly. *Physical Review E* **2007**, *76*, 021119.
- (53) Nguyen, H. D.; Reddy, V. S.; Brooks, C. L. Deciphering the Kinetic Mechanism of Spontaneous Self-Assembly of Icosahedral Capsids. *Nano Letters* **2007**, *7*, 338–344.
- (54) Rapaport, D. C. Self-Assembly of Polyhedral Shells: A Molecular Dynamics Study. *Physical Review E* **2004**, *70*, 051905.
- (55) Rapaport, D. C. Role of Reversibility in Viral Capsid Growth: A Paradigm for Self-Assembly. *Physical Review Letters* **2008**, *101*, 186101.
- (56) Krishna, V.; Ayton, G. S.; Voth, G. A. Role of Protein Interactions in Defining HIV-1 Viral Capsid Shape and Stability: A Coarse-Grained Analysis. *Biophysical Journal* **2010**, *98*, 18–26.

- (57) Perlmutter, J. D.; Hagan, M. F. Mechanisms of Virus Assembly. *Annual Review of Physical Chemistry* **2015**, *66*, 217–239.
- (58) Pak, A. J.; Grime, J. M. A.; Yu, A.; Voth, G. A. Off-Pathway Assembly: A Broad-Spectrum Mechanism of Action for Drugs That Undermine Controlled HIV-1 Viral Capsid Formation. *Journal of the American Chemical Society* **2019**, *141*, 10214–10224.
- (59) Hagan, M. F.; Grason, G. M. Equilibrium Mechanisms of Self-Limiting Assembly. *Reviews of Modern Physics* **2021**, *93*, 025008.
- (60) Kashchiev, D.; Vekilov, P. G.; Kolomeisky, A. B. Kinetics of Two-Step Nucleation of Crystals. *The Journal of Chemical Physics* **2005**, *122*, 244706.
- (61) De Yoreo, J. J.; Gilbert, P. U. P. A.; Sommerdijk, N. A. J. M.; Penn, R. L.; Whitlam, S.; Joester, D.; Zhang, H.; Rimer, J. D.; Navrotsky, A.; Banfield, J. F.; Wallace, A. F.; Michel, F. M.; Meldrum, F. C.; Cölfen, H.; Dove, P. M. Crystallization by Particle Attachment in Synthetic, Biogenic, and Geologic Environments. *Science* **2015**, *349*, aaa6760.
- (62) Dogan, J.; Gianni, S.; Jemth, P. The Binding Mechanisms of Intrinsically Disordered Proteins. *Phys. Chem. Chem. Phys.* **2014**, *16*, 6323–6331.
- (63) Wilson, C. J.; Bommarius, A. S.; Champion, J. A.; Chernoff, Y. O.; Lynn, D. G.; Paravastu, A. K.; Liang, C.; Hsieh, M.-C.; Heemstra, J. M. Biomolecular Assemblies: Moving from Observation to Predictive Design. *Chemical Reviews* **2018**, *118*, 11519–11574.
- (64) Sherman, Z. M.; Swan, J. W. Dynamic, Directed Self-Assembly of Nanoparticles *via* Toggled Interactions. *ACS Nano* **2016**, *10*, 5260–5271.
- (65) Sherman, Z. M.; Swan, J. W. Transmutable Colloidal Crystals and Active Phase Separation *via* Dynamic, Directed Self-Assembly with Toggled External Fields. *ACS Nano* **2019**, *13*, 764–771.
- (66) Savage, J. R.; Dinsmore, A. D. Experimental Evidence for Two-Step Nucleation in Colloidal Crystallization. *Physical Review Letters* **2009**, *102*, 198302.